ELSEVIER

Surface Science 391 (1997) 150–160

surface science

Molecular dynamics simulations for xenon adsorption on Pt(111): dynamical differences in the effects produced by the Barker–Rettner and Morse potentials

Jason F. Weaver, James A. Stinnett, Robert J. Madix *

Department of Chemical Engineering, Stanford University, Stanford, CA 94305, USA

Received 26 August 1996; accepted for publication 8 May 1997

Abstract

In order to gain a better insight into the effects of gas–surface potential functions and on observable quantities related to adsorption, xenon trapping on cold Pt(111) was simulated using classical three-dimensional stochastic trajectory calculations with a pairwise additive Morse potential and a potential developed by Barker and Rettner [J. Chem. Phys. 97 (1992) 5844]. Both potentials predict the same dependence of the initial trapping probability on the translational energy and angle of incidence of the colliding xenon atoms, but only the Barker–Rettner potential gives agreement with the observed in-plane scattered distributions, thus providing a basis for distinguishing the potentials. The features of the potentials that determine the differences in collisional dynamics are the potential corrugation and the steepness of the repulsive wall. Corrugation causes substantial scrambling between the components of incident gas-atom parallel and normal momentum, whereas the impulsiveness of the collisions determines the efficiency of energy transfer between the gas and surface. Long collision times computed for the softer Morse potential result in secondary surface recoil effects which cause scattering xenon atoms to gain normal momentum from the vibrationally excited surface; these effects are absent in the impulsive Barker–Rettner potential. These differences in the microscopic dynamics predicted by the potentials strongly effect the computed scattering distributions, but are compensatory in predicting the initial trapping probabilities. The Barker–Rettner potential behaves much like traditional hard cube models, whereas the Morse potential predicts that the efficacious dissipation of incident parallel momentum to the surface facilitates trapping at glancing incidence. © 1997 Elsevier Science B.V.

Keywords: Adsorption kinetics; Atom–solid interactions; Computer simulations; Molecular dynamics; Platinum

1. Introduction

Recently, Barker and Rettner (BR) [1] developed an empirical potential for the xenon–Pt(111) interaction which accurately reproduces a wide variety of experimental observations, including the commensurate-to-incommensurate phase transition at high Xe coverages, Xe desorption rates, the energy and angular dependencies of the initial trapping probability, and the angular distributions of scattered species over a wide range of incident kinetic energies. The truly remarkable aspect of this potential is its ability to reproduce such a wide variety of behavior.

Other potentials have appeared in the literature which also accurately reproduce subsets of the behavior exhibited by xenon on Pt(111) [2–10]. There is, in general, a need for reliable potentials

* Corresponding author. Fax: (+1) 415 723 9780; e-mail: rjm@rio.stanford.edu

PII S0039-6028(97)00478-0

in order to predict the details of molecular adsorption and scattering. In this paper we have examined the collisional dynamics predicted by both the BR potential and a Morse potential [10] in order to determine (1) the dynamical features of the scattering predicted by the BR potential, and (2) the differences in the scattering dynamics that arise from different potential functions, which can serve as a guide to distinguishing correct and incorrect potential functions. In this case, these potentials lead to nearly the same prediction of the initial trapping probabilities, but predict vastly different angular and final energy distributions of the scattered atoms. It is thus the latter observables that lead to a distinction between the validity of the two potentials. It may therefore be concluded that, in general, agreement between theory and experiment on the energy scaling is an insufficient test of the accuracy of the potential.

2. Simulation methods

The stochastic, three-dimensional classical mechanical trajectory technique has been described in detail previously [11,12]. Periodic boundary conditions were imposed in the x and y directions parallel to the surface plane to create an infinite surface. A Pt(111) slab consisting of three layers each with 36 atoms was coupled to the bulk by friction, random and constraint forces applied to the bottom layer of the slab. In fact, for the collisional energies studied here, the presence of the heat bath was relatively unimportant, as its elimination produced no changes in the calculated initial trapping probabilities to within the statistical uncertainty of ± 0.02.

2.1. Pt–Pt potential

The platinum atoms were chosen to vibrate about their bulk-terminated equilibrium positions (Pt–Pt bond length 2.769 Å). Following the simple prescription by Adelman and Doll [13], the Pt–Pt interactions were represented by nearest neighbor (NN) and next nearest neighbor (NNN) harmonic force constants taken from previous work ($k_{NN}=43.6$ kg s^{-2}, $k_{NNN}=10.2$ kg s^{-2}) [10,14] and the friction constant applied to the third layer atoms in the z direction was 1.86×10^{13} s^{-1}. These slab parameters accurately reproduce the bulk Pt Debye temperature of 234 K [15]. The resulting surface Debye temperature of 124 K, however, is slightly higher than the experimental value of 110 K [16].

2.2. Xe–Pt interaction potentials

The potential developed by BR consists of both additive and non-additive terms. In order to fit the wide variety of observations for the Xe/Pt(111) system the BR potential contains nine adjustable parameters, the values of which are given elsewhere [1]. The BR potential takes the following form:

$$U=\sum[u(R_i)+v(R_i')]+V(z_g^{av})$$

where

$$u(R_i)=A_1\exp(-\alpha_1 R_i)$$

and

$$v(R_i')=-c_6 G(R_i')/R_i'^6$$

with R_i defined as in the Morse potential and R_i' is centered a distance h above the Pt atom at position (x_i,y_i,z_i) and is defined as

$$R_i'^2=(x_g-x_i)^2+(y_g-y_i)^2+(z_g-z_i-h)^2$$

where the gas atom position is specified by the coordinates (x_g, y_g, z_g) and is referenced to the same fixed coordinate system as the Pt atoms.

The damping function $G(R)$ is defined by

$$G(R)=1,\quad R>R_1,$$

and

$$G(R)=\exp[-(R_1/R-1)^2],\quad R\le R_1,$$

where R_1 is an adjustable parameter.

The non-additive term $V(z_g^{av})$ is defined by

$$V(z_g^{av})=AW\exp(-\alpha z_g^{av})/[W+A\exp(-\alpha z_g^{av})]$$

where z_g^{av} is defined as the height relative to the "local-average" surface

$$z_g^{av}=z_g-z_{gs}^{av}.$$

The position of the local surface z_{gs}^{av} is a weighted

average over surface atoms

$$z_{gs}^{av} = \sum'[z_i\phi(R_i)]/\sum[\phi(R_i)]$$

where the primed summation indicates that the sum is to be performed only for surface atoms. The weighting function is given by

$$\phi(R) = \exp(-\delta R^2)$$

where δ is another adjustable parameter.

As described by BR [1] the use of a non-additive, z-dependent term in the Xe/Pt(111) potential is intended to account for the repulsive interactions between the xenon atom and the delocalized conduction electrons of the metal. A local-average surface is defined in order that the repulsive force resulting from the non-additive term is predominantly transmitted to the Pt atoms closest to the incident xenon atom, thereby allowing for realistic energy dissipation through vibrational excitation of the immediate surface atoms. In the low energy repulsive portion of the potential the non-additive term dominates over the central force repulsive interaction, especially above threefold hollow sites, resulting in a relatively smooth potential energy surface topography. This smoothed interaction was necessary to reproduce the narrow angular distributions observed in low energy scattering. A similar smoothed potential was used by Tully [2] in calculating angular and velocity distributions from low energy scattering for the Xe/Pt(111) system.

For the pairwise additive Morse potential a cut-off distance r_c of 9.0 Å was applied for convenience and a background term fit to a Gaussian was incorporated to account for the long-range attractive interactions between the xenon atom and the bulk solid atoms not explicitly included in the sum of pairwise potentials. For this case, the total potential energy function takes the form

$$\begin{aligned} U = &\sum \epsilon\{\exp[-2\sigma(R_i - r_0)] - 2\exp[-\sigma(R_i - r_0)]\} \\ &- N\epsilon\{\exp[-2\sigma(r_c - r_0)] - 2\exp[-\sigma(r_c - r_0)]\} \\ &- \alpha\exp(-\beta z^2) \end{aligned} \quad (1)$$

where R_i is taken to be the distance between the Xe atom and the ith Pt atom, or r_c, whichever is smaller. The second term in Eq. (1) ensures that the potential is continuous at $R_i = r_c$. The background term was obtained by determining the contribution to the total binding energy of a large number of Pt atoms not included in the sum over the atoms in the slab. The resulting term was found to be only a function of the height above the surface z, and could be adequately fit by a Gaussian. As described previously [10], this term is unimportant because the Morse potential is a relatively short-range interaction, but it was included for consistency. A consequence of the short-range interaction is that the Morse potential does not accurately represent the correct $-C/z^3$ asymptotic behavior of a gas–surface potential. However, precise description of the long-range behavior of the potential is not essential in determining energy transfer occurring in gas–surface collisions due to the weak coupling between gas and surface atom motions at large separations [17].

There are three parameters in the Morse potential which can be adjusted independently: ϵ the well depth; σ the range parameter; r_0 the equilibrium separation. Given values for σ and r_0, ϵ is chosen such that the potential reproduces the experimental binding energy of 25.9 kJ mol^{-1} as determined by TPD measurements [18]. This restriction reduces the number of parameters which can be adjusted to match the experimental gas–surface dynamics. The optimum set of Morse potential parameters which fit the dependence of the initial trapping probability of Xe on Pt(111) on incident energy and angle were determined by Arumainayagam et al. to be $\epsilon = 2.628$ kJ mol^{-1}, $\sigma = 1.05$ Å^{-1} and $r_0 = 3.20$ Å [10].

Fig. 1 illustrates the potential curves as a function of height above atop and hollow sites for both the Morse and BR potentials. Some important differences are immediately apparent. The equilibrium locations and heights differ for the potentials. The BR potential has the equilibrium position located at a height of 3.3 Å above an atop site, though the energy difference between atop and hollow sites is small. This height is in good agreement with previous calculations [19–21]. The Morse potential has its energy minimum located above a hollow site at a height of 2.3 Å. The details of the potential minima affect the equilibrium behavior, however; the differences which

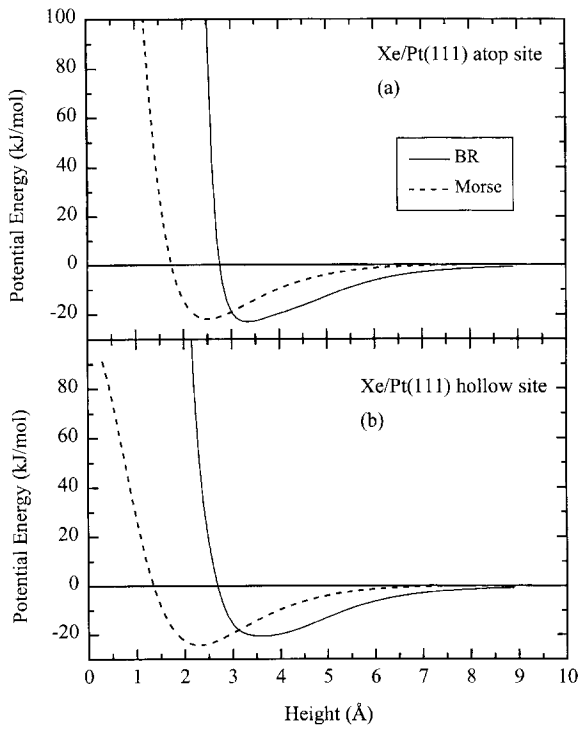

Fig. 1. BR and Morse potential energy curves as a function of height above (a) an atop site and (b) a threefold hollow site. The solid lines are for the BR potential and the dashed lines are for the Morse.

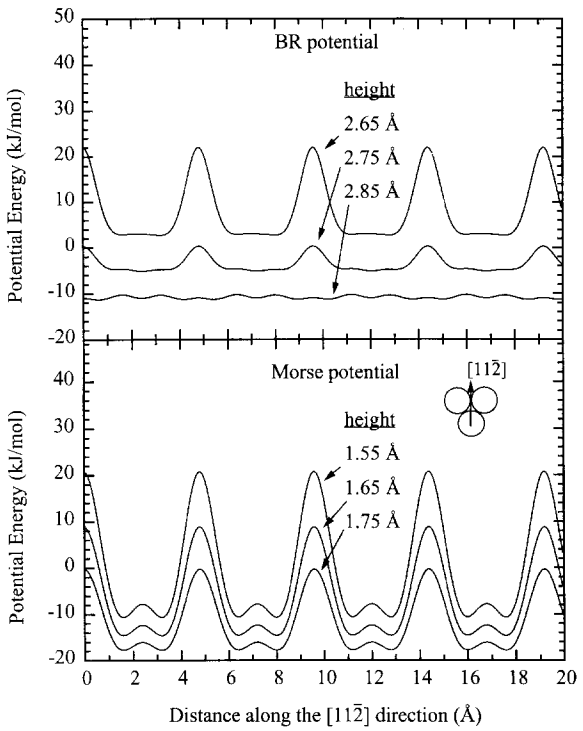

Fig. 2. Lateral variation of the potential energy in the [11$\bar{2}$] direction above a static Pt(111) surface. Three potential-energy contours are displayed for (a) the BR potential at constant xenon atom heights of 2.65 Å, 2.75 Å and 2.85 Å and for (b) the Morse potential at constant xenon atom heights of 1.55 Å, 1.65 Å and 1.75 Å. The inset displays the [11$\bar{2}$] direction on a Pt(111) surface. The smallest heights, corresponding to 2.65 Å and 1.55 Å for the BR and Morse potentials respectively, were chosen to yield a potential energy of about 20 kJ mol^{-1} above an atop site. For subsequent energy contours the xenon atom height is systematically increased by 0.1 Å to illustrate how the corrugation varies throughout the region in which a low energy (20 kJ mol^{-1}) xenon atom exchanges energy with the surface.

influence energy exchange occur in the repulsive regions.

A comparison of the potentials (Fig. 1) also indicates that the BR potential exhibits a "harder" repulsive wall than the Morse potential over either the hollow or atop sites, and this difference is accentuated for the hollow site. The increased steepness of the BR repulsive region results in collisions that are more impulsive than those described by Morse interactions. This difference has important consequences in the energy exchange during the gas–surface collision and, therefore, on the predicted dynamics of trapping.

The corrugations in the repulsive regions of the potentials are also different. Fig. 2 displays the potential energy as a function of lateral position in the [11$\bar{2}$] direction for both potentials at different heights of the xenon atom above the surface. At these heights the potential felt by a xenon atom incident with 20 kJ mol^{-1} kinetic energy is much more corrugated for the Morse potential than for the BR potential, and the corrugation of the Morse potential decreases more slowly than the BR potential with increasing distance from the surface. Moreover, at the closest point of impact a xenon atom will have less energy than it initially possessed, since energy is dissipated to the surface during the collision. The loss of momentum to the surface prevents the incident atom from encountering the larger corrugation at distances closer to the surface that would result from an elastic collision. Hence, the actual corrugation

experienced by a xenon atom initially with 20 kJ mol^{-1} kinetic energy is typically less than the largest corrugation displayed in Fig. 2, particularly for the BR potential. For the BR potential, for example, at the distance of closest approach the average energy calculated for 2500 xenon atom trajectories initially with 18 kJ mol^{-1} translational energy at normal incidence is about 6 kJ mol^{-1}. Consequently, the differences in corrugation between these potential functions will strongly influence the model-based interpretation of the effects of different energy exchange processes on trapping, e.g. the role of parallel momentum exchange.

2.3. Calculation methods

Newton's equations of motion governed by the interactions described above were integrated by a modified Beeman algorithm with a time step of 2 fs [22]. The initial gas atom translational energy and angle of incidence were chosen to match previous experimental conditions [1,10]. The initial positions and momenta of the surface atoms were chosen for each trajectory at random from a Boltzmann distribution at a prescribed surface temperature. For this study the surface temperature was kept at 95 K for the calculations of the trapping probabilities and was increased to 800 K for the calculation of scattered angular and energy distributions. Random forces at each integration step were selected from a Gaussian distribution which rigorously satisfies the fluctuation-dissipation theorem, as described previously [11].

Xenon atoms were initially located outside of the range of the gas–surface interaction at a height of 9.5 Å above the surface. Although a cut-off distance was not employed for the BR potential, this starting height is sufficiently far from the surface to make the initial gas–surface interaction insignificant. The initial x and y positions of the atom were chosen from a 50×50 grid covering the entire surface plane. The use of the grid was chosen for convenience and does not alter the computed trapping probabilities from those obtained using a uniform random distribution.

Trajectories were integrated until one of the three following conditions occurred: (1) the xenon atom scattered from the surface and escaped to a height of 9.0 Å above the surface (the potential cut-off of the Morse potential) and had an amount of perpendicular translational energy in excess of its potential energy at that height. These trajectories were classified as scattered; (2) if the xenon total energy (kinetic plus potential) fell below a specific energy selected to be the trapping criterion, which was set at $-5k_BT_s$ in this study, these trajectories were designated as trapped. It is noted that changing the trapping criterion to $-2k_BT_s$ had virtually no effect on the computed trapping probabilities; (3) if neither (1) or (2) resulted after the 15 000 integration steps (30 ps) the trajectory was terminated and classified as uncertain. The largest number of uncertain trajectories for either potential was obtained at the highest incident energy (50 kJ mol^{-1}) employed and at 60° incidence. At these incident conditions 7% (184) of the 2500 Morse trajectories were classified as uncertain, whereas none of the BR trajectories could be designated as trapped during the 15 000 time steps (30 ps). Hence, the uncertain trajectories were classified as trapped, as it seems quite unlikely that any of these could scatter after such a long interaction time with the surface. This is supported strongly by the infrequency of multiple bounce scattering that was observed for either potential after more than about five bounces. For consistency, the uncertain trajectories determined using the Morse interaction were also included as trapped in the analysis. The number of trajectories used in the trapping calculations was 2500, yielding a statistical uncertainty of ± 0.02 in the computed trapping probability. To obtain good statistics for the in-plane scattered distributions it was necessary to integrate 15 000 trajectories and include atoms that scattered within $\pm 2.5°$ of the scattering plane.

3. Simulation results

The energy scaling and magnitudes of the initial trapping probabilities computed from the potential parameters cited above are the same for both potentials. The initial trapping probabilities predicted by the Morse and BR potentials are plotted in Fig. 3 as a function of $E_i \cos^n(\theta_i)$ for $n = 1.8$

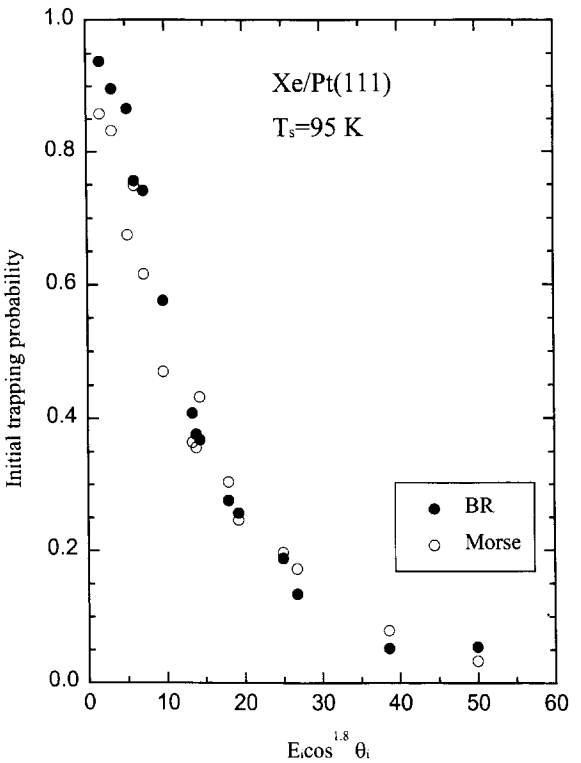

Fig. 3. The initial trapping probability of xenon trapping on Pt(111) plotted as a function of $E_i \cos^{1.8}\theta_i$ for $6 \le E_i \le 50$ kJ mol^{-1} and $0 \le \theta_i \le 60°$. The open circles represent calculations using the Morse potential and the solid circles are for calculations using the BR potential. The surface temperature is 95 K.

where E_i is the incident energy and θ_i is the angle of incidence from the surface normal. For each potential, the value of $n = 1.8$ was determined to be the best scaling exponent which would collapse the data to a universal curve. The predicted initial trapping probabilities are in excellent agreement with the experimental data reported by BR [1]. The "energy scaling" in which n takes on a value of two would be predicted by the so-called hard cube models [23,24], which assume that momentum of the gas atom tangential to the surface is conserved upon impact and that only energy associated with the normal component of momentum must be dissipated in order for trapping to take place. In view of the assumptions of the hard cube models, it is often asserted that a value of n close to two indicates that the corrugation of the gas–surface interaction is small over the low energy range at which trapping occurs. Clearly, this is not the case for the Morse potential, which is corrugated in the low energy repulsive regime.

The angular and energy distributions of xenon atoms inelastically scattered from a Pt(111) surface exhibit significant differences for the two potentials (Figs. 4 and 5); the dynamics predicted by the Morse potential do not adequately reproduce the experimental data. For example, the BR potential accurately predicts superspecular angular distributions that are consistent with scattering from a flat surface, in good agreement with experimental data [1], whereas the Morse potential predicts broader subspecular angular distributions (Figs. 4a and 5a). For an incident kinetic energy of 48.3 kJ mol^{-1} and $\theta_i = 45°$ (Fig. 4b), the BR potential predicts that atoms which scatter superspecularly have relative kinetic energies less than

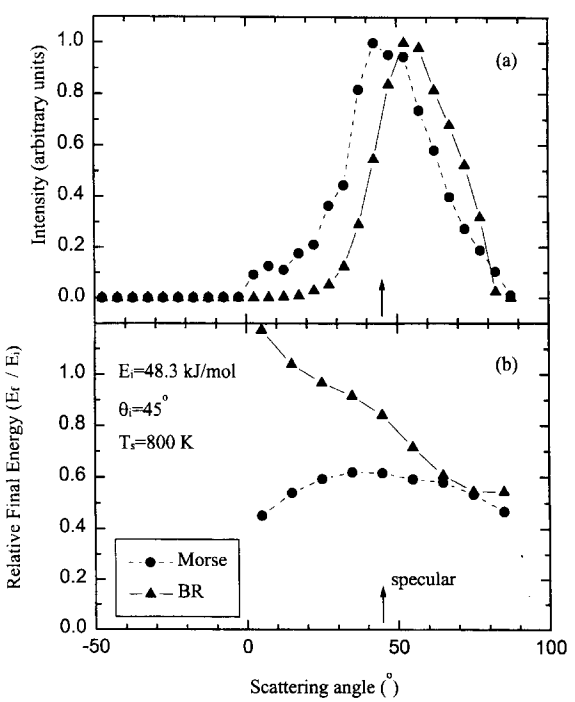

Fig. 4. (a) In-plane intensity and (b) average final translational energy distributions as a function of scattering angle for xenon scattered from Pt(111). The solid circles represent calculations using the Morse potential and the solid triangles are for the BR potential. The xenon initial conditions are $E_i = 48$ kJ mol^{-1} and $\theta_i = 45°$ and the surface temperature is 800 K.

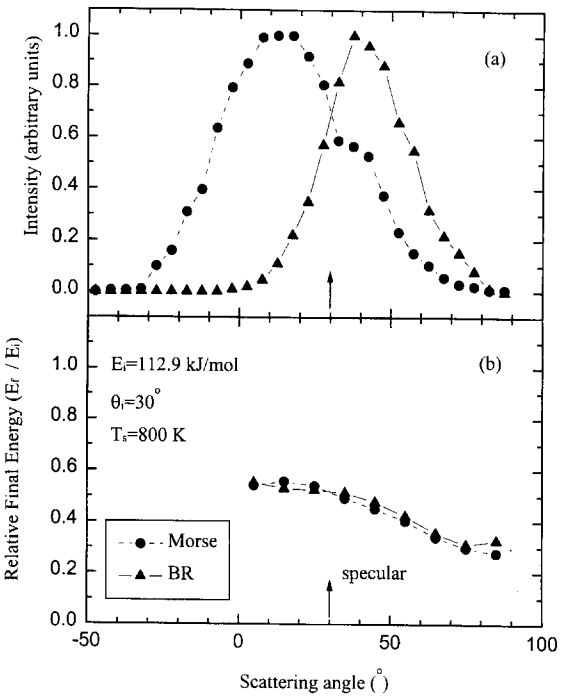

Fig. 5. (a) In-plane intensity and (b) average final translational energy distributions as a function of scattering angle for xenon scattered from Pt(111). The solid circles represent calculations using the Morse potential and the solid triangles are for the BR potential. The xenon initial conditions are $E_i = 113$ kJ mol^{-1} and $\theta_i = 30°$ and the surface temperature is 800 K.

unity, whereas those that scatter subspecularly have relative kinetic energies in excess of one. This behavior is expected if mostly normal momentum is dissipated to the surface. The effects of the corrugation produced by the Morse potential are evident in both the broad angular distributions and the final energy distributions (Fig. 4b), in which the final energies are only weakly correlated with the exit angles. For the higher incident energy conditions ($E_i = 112.9$ kJ mol^{-1}, $\theta_i = 30°$) the final energies of the scattered BR and Morse trajectories depend similarly on exit angle (Fig. 5b); however, the higher Morse corrugation again leads to subspecular scattering, whereas the BR produces superspecular behavior (Fig. 5a). The calculations show that the in-plane energy and intensity distributions are highly dependent on the details of the potential, and provide an assessment of the accuracy of the potential function – for any potential function. Comparison of the calculated and experimental scattering distributions in this case shows that the actual corrugation of the interaction is overestimated by the Morse potential.

4. Discussion and analysis

In order to facilitate a deeper understanding of the differences in these two potential functions in describing the adsorption and scattering dynamics, the analysis was carried to a higher order of detail. Since it is known that trapping is determined primarily by energy exchange on the first bounce, the partitioning of energy after the first bounce for many gas–surface collisions was determined. For each of 2500 trajectories incident with a fixed energy and angle, the parallel, perpendicular and total translational energies of the xenon atom after the first bounce and at the classical outer turning point were stored for analysis [25]. The perpendicular energy is defined as the sum of the perpendicular translational and potential energy. Once all 2500 trajectories were completed, translational energy distributions were computed by arranging the total number of trajectories into 30 different bins according to the amount of parallel, perpendicular or total translational energy possessed by a xenon atom after the first bounce at the outer turning point. The translational energy distributions after the first bounce were also designated by the trajectories that eventually trapped or scattered. Energy loss distributions were easily obtained from the total translational energy distributions by subtracting the initial energy. Both averages and standard deviations were calculated for each distribution.

4.1. Trapping dynamics

It is interesting to examine how the two potentials can lead to almost the same trapping probabilities and the same energy scaling, even though the dynamics of the processes are quite different. The dynamics accompanying the BR potential are very similar to that expected of a hard cube model. At the incident energies where trapping is significant the BR potential is flat and the repulsive wall is

steep; as a result, only the exchange of incident normal energy with the surface produces trapping. For example, at normal incidence and 18 kJ mol^{-1} initial translational energy the computed BR trajectories gain only negligible parallel momentum since the corrugation encountered is small. The atoms that eventually trap lose an average of about 22 kJ mol^{-1} to the surface on the first bounce, resulting in a final energy that is in the attractive region of the potential. Likewise, at glancing incidence (60° from the surface normal) the initial parallel energy is nearly conserved for all BR trajectories with 18 kJ mol^{-1} initial total energy (Fig. 6a). Trapping occurs only when the energy lost to the surface during the first bounce is greater than the initial 4.5 kJ mol^{-1} of normal energy (Fig. 6b). Hence, scattering results almost solely from collisions in which insufficient normal momentum is transferred to the surface to contain the xenon atoms in the attractive well. The near-normal energy scaling produced by the BR potential is the direct consequence of the absence of corrugation and the impulsiveness of the net interaction potential, which is clearly shown in the collisional dynamics.

Interestingly, near-normal energy scaling is also predicted for the Morse interaction, despite the predominant role of parallel momentum exchange in the collisions. This result is surprising, since it is usually expected that collisions with a corrugated surface will produce non-normal energy scaling as a result of mixing parallel and perpendicular momentum [26]. Indeed, the Morse interaction does predict that parallel and perpendicular momentum are exchanged during some collisions. A gain in parallel momentum during the first bounce is found to assist trapping for both glancing and normal incident trajectories. In addition, nearly all atoms incident with 18 kJ mol^{-1} total energy at glancing angles (60°) which are scattered lose parallel energy; however, even for many atoms which are trapped, parallel energy is lost (Fig. 6c). The high efficiency with which parallel energy is dissipated to the surface significantly lowers the fraction of trajectories that scatter via conversion of parallel to perpendicular momentum. For example, at 60° incidence about 45% of all trajectories lose parallel energy during the initial collision but

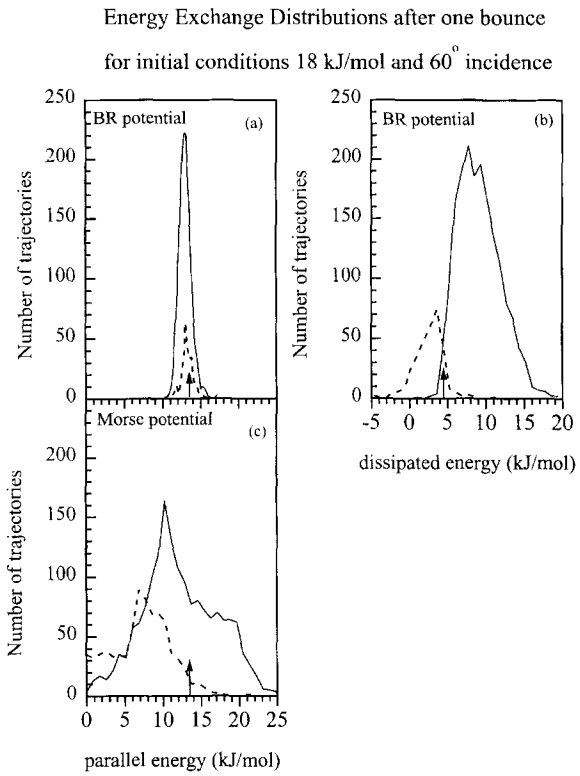

Fig. 6. Energy distributions after the first bounce for trapped (solid lines) and scattered (dashed lines) trajectories which represent (a) the parallel energy and (b) the energy lost to the surface for BR trajectories; (c) the parallel energy for Morse trajectories. All 2500 xenon atoms are incident on Pt(111) with 18 kJ mol^{-1} initial translational energy at an angle of 60° from the surface normal and for a surface temperature of 95 K. In (a) and (c) each arrow indicates the initial parallel energy (13.5 kJ mol^{-1}) of the atoms and, in (b) the arrow indicates the initial normal energy (4.5 kJ mol^{-1}).

still lead to trapping (Fig. 6c), indicating that a significant fraction of the initial parallel momentum for these trajectories is dissipated to the surface. The effectiveness of parallel energy dissipation to the surface ultimately leads to an enhancement in the trapping probability at glancing incidence, compared with normal incidence, and hence to the prediction of near-normal energy scaling of the initial trapping probabilities.

4.2. Site dependence

The distribution of impact sites resulting in either trapping or scattering at a given incident

angle and energy is also significantly different for the two potentials. Distributions were constructed for each potential for trajectories at 60° incidence and 18 kJ mol^{-1} initial energy that scatter. The site maps are displayed in hexagonal Wigner–Seitz cells, in which the center is an atop site and the vertices represent the six adjacent threefold hollow sites (Fig. 7). For the BR potential, scattering results from the collisions near bridge and hollow sites where energy transfer is the least efficient (Fig. 7a). In addition, since parallel momentum is nearly conserved, the impact sites for scattering are almost symmetrically distributed about the perimeter of the Wigner–Seitz cell. As illustrated by the site map, the dynamical behavior produced by the smooth BR potential results in superspecular scattering (Figs. 4a and 5a) for low incident energies.

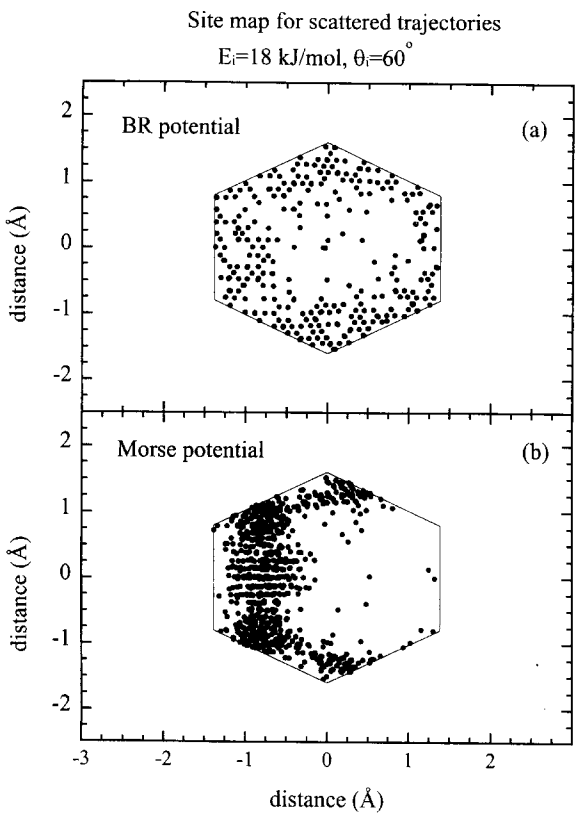

Fig. 7. Lateral positions at the inner turning points of (a) scattered BR trajectories and (b) scattered Morse trajectories. All xenon atoms are incident on Pt(111) initially with 18 kJ mol^{-1} translational energy and at an angle of 60° from the surface normal and for a surface temperature of 95 K. Each dot represents the impact point of a single trajectory and the atop site is located at the center of the cell. The total number of scattered BR and Morse trajectories at these incident conditions are 335 and 813 respectively.

For the Morse trajectories, scattering occurs mostly from the leading face where the effect of the corrugation is the strongest (Fig. 7b). In this case, atoms are scattered in the subspecular direction by directly converting incident parallel to normal momentum. Scattering from the corrugation also tends to broaden the angular distributions, particularly at high kinetic energies (Fig. 5a), since the lateral forces vary significantly across the surface unit cell.

4.3. Surface recoil

One of the most dramatically different features of the scattering dynamics produced by the two potentials is the role of multiple collisions in trapping and scattering. Hard cube models predict multiple collisions for gas–surface atom pairs with mass ratios exceeding 0.33 and have, therefore, been assumed useless for the description of such collisions [23]. For the Morse interaction, recoil of the surface Pt atom initially struck in a collision occurs during the collisional time scale and produces a secondary collision with the xenon atom during its departure from the surface. In the BR potential these recoil collisions are absent in the range of incident kinetic energies explored in this work. The existence of these secondary collisions for the Morse trajectories and their absence for the BR trajectories can be attributed to the differences in the collisional times, which are determined by the steepness of the repulsive parts of the potentials and which are longer for the Morse interaction. A similar recoil effect has also been observed in a simulation of high energy xenon scattering from GaAs(110) [27].

A consequence of the surface recoil is a transfer of energy from the lattice back to the xenon atom as it departs from the surface, thereby reducing the net energy dissipation in the collision. For all Morse trajectories incident with 18 kJ mol^{-1} translational energy and at normal or 60° incidence the average recoil energies are found to be

6.5 kJ mol^{-1} and 4.8 kJ mol^{-1} respectively (Fig. 8a). Independent of the incident angle, about 90% of this recoil energy is channeled into the perpendicular energy of the xenon atom. Since there is only a marginal dependence of the recoil energy on the angle of incidence, the energy scaling exponent would change negligibly in the absence of recoil. However, the recoil phenomenon does reduce the net energy transfer to the surface, leading to a reduction in the initial trapping probability. For xenon initially with 18 kJ mol^{-1} translational energy and without recoil, the initial trapping probability would be greatly overestimated.

Secondary surface recoil also has a significant effect on the angular intensity distributions of scattered atoms. Since most of the recoil energy is transferred normal to the surface, the final exiting angles of scattered atoms are shifted towards the surface normal due to recoil. For example, without recoil the angular distributions predicted by the Morse potential shift by 8.2° and 20.5° towards the superspecular direction for initial conditions of 112.9 kJ mol^{-1} and 30° incidence and 48.3 kJ mol^{-1} and 45° incidence respectively, each at a surface temperature of 800 K, rendering their peak maxima nearly identical to the angular distributions predicted by the BR potential. Thus, the subspecular scattering predicted by the Morse potential results mainly from the secondary recoil of the surface, rather than from the corrugation.

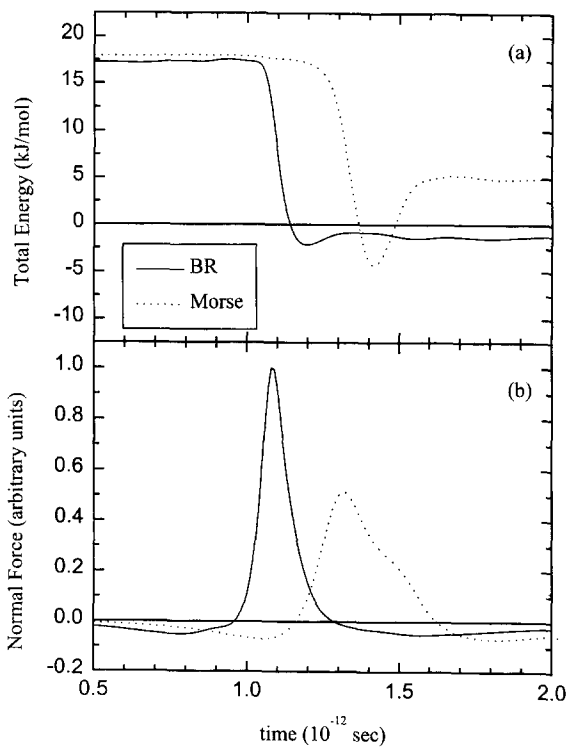

Fig. 8. Time progression of (a) the total energy and (b) the normal forces on the xenon atom for a xenon atom single trajectory. The xenon atom is incident on the Pt(111) surface at normal incidence and initially with 18 kJ mol^{-1} translational energy. The trajectory begins at a lateral position 0.7994 Å from an atop site and midway between an atop and hollow site. The solid lines represent the BR trajectory and the dashed lines are for the Morse trajectory.

4.4. Representative single trajectories

The magnitude and duration of the normal forces acting on an incident xenon atom during the collision govern the energy transfer to the surface and the influence of the secondary recoil of the surface atoms. A comparison of trajectories computed using the BR and Morse potentials is shown in Fig. 8. The two trajectories were each initiated with 18 kJ mol^{-1} initial energy, at normal incidence and for an impact site 0.800 Å from the atop site and midway between the hollow and atop site. The total energy and normal forces for these trajectories are plotted as a function of time in Fig. 8. Prior to surface recoil, energy transfer is nearly equally as efficient for each trajectory (Fig. 8a), even though the BR repulsive forces are larger than those of the Morse. The duration of the repulsive force is critical in determining the effect of recoil on the initial energy transfer to the surface; the durations are 330 fs and 470 fs for the BR and Morse potentials respectively (Fig. 8b). The fastest vibrations of the surface atoms yield a vibrational time of about 387 fs, according to the computed surface Debye temperature [25]. Hence, secondary surface recoil significantly affects the Morse trajectories because the collisional time is longer than the shortest characteristic time for vibration. Conversely, the atoms in the BR trajectories escape the surface without secondary collisions.

5. Conclusions

Dynamical calculations using the BR and Morse potentials produce drastically different dynamical behavior on the microscopic level. However, manifestations of these differences are less evident in the computed observable quantities. By comparison with experiment, only the in-plane scattering distributions establish the accuracy of the low energy, repulsive region of the BR potential over that of the Morse potential. For the Morse interaction, the effects of secondary recoil primarily determine the deviations between the computed and experimental angular distributions for low energy scattering. Without this effect, the predictions of the potential functions would be nearly indistinguishable. It is important to recognize that the scattering distributions are a sensitive probe of the underlying collisional dynamics, and should, therefore, be considered an essential test for the assessment of accurate gas–surface potential energy functions.

Acknowledgements

We are grateful to Dr. John Tully and Dr. Martin Head-Gordon for providing us with the initial computer code used for the simulations. We are also thankful to Professor George Homsy and Dr. Michael Spaid for use of an IBM Risc/6000 workstation to perform some of these calculations. Financial support for this work was provided by the Department of Energy, Chemical Sciences Division, Office of Basic Energy Sciences (grant DE-FG03-86ER13468).

References

[1] J.A. Barker, C.T. Rettner, J. Chem. Phys. 97 (1992) 5844.
[2] J.C. Tully, Faraday Discuss. Chem. Soc. 80 (1985) 291.
[3] J.C. Tully, Surf. Sci. 111 (1981) 461.
[4] E.K. Grimmelmann, J.C. Tully, E. Helfand, J. Chem. Phys. 74 (1981) 5300.
[5] P.A. Rejto, H.C. Andersen, J. Chem. Phys. 98 (1993) 7636.
[6] F. de Jong, A.P.J. Jansen, Surf. Sci. 317 (1994) 1.
[7] A.P.J. Jansen, J. Chem. Phys. 97 (1992) 5205.
[8] A.P.J. Jansen, Surf. Sci. 272 (1992) 193.
[9] D.S. Bethune, J.A. Barker, C.T. Rettner, J. Chem. Phys. 92 (1990) 6847.
[10] C.R. Arumainayagam, R.J. Madix, M.C. McMaster, V.M. Suzawa, J.C. Tully, Surf. Sci. 226 (1990) 180.
[11] J.C. Tully, Acc. Chem. Res. 14 (1981) 188.
[12] J.C. Tully, in: D. Langreth, H. Suhl (Eds.), Many Body Phenomena at Surfaces, Academic Press, New York, 1984, p. 377.
[13] S.A. Adelman, J.D. Doll, J. Chem. Phys. 64 (1976) 2375.
[14] M. Head-Gordon, J.C. Tully, C.T. Rettner, B. Mullins, D.J. Auerbach, J. Chem. Phys. 94 (1991) 1516.
[15] J.R. Harris, N. Benczer-Koller, G.M. Rothberg, Phys. Rev. A 137 (1965) 1101.
[16] H.B. Lyons, G.A. Somorjai, J. Chem. Phys. 44 (1966) 3707.
[17] J. Harris, in: C.T. Rettner, M.N.R. Ashfold (Eds.), Dynamics of Gas–Surface Interactions, Royal Society of Chemistry, Cambridge, 1991, p. 9.
[18] B. Poelsema, L.K. Verheij, G. Comsa, Surf. Sci. 152 153 (1985) 851.
[19] J.E. Muller, Phys. Rev. Lett. 65 (1990) 3021.
[20] J.E. Black, R.A. Janzen, Phys. Rev. B 38 (1988) 8494.
[21] J.E. Black, R.A. Janzen, Phys. Rev. B 39 (1989) 6238.
[22] J.C. Tully, G.H. Gilmer, M. Shugard, J. Chem. Phys. 71 (1979) 1630.
[23] R.M. Logan, R.E. Stickney, J. Chem. Phys. 44 (1966) 195.
[24] R.M. Logan, J.C. Keck, J. Chem. Phys. 49 (1968) 860.
[25] J.A. Stinnett, R.J. Madix, J.C. Tully, J. Chem. Phys. 104 (1996) 3134.
[26] J.A. Stinnett, J.F. Weaver, R.J. Madix, Surf. Sci. 380 (1997) 489.
[27] C. Lim, J.C. Tully, A. Amirav, P. Trevor, M.J. Cardillo, J. Chem. Phys. 87 (1987) 1808.